ELSEVIER

International Journal of Mass Spectrometry 223–224 (2003) 579–597

International Journal of Mass Spectrometry

www.elsevier.com/locate/ijms

Modeling of ultrasoft X-ray induced DNA damage using structured higher order DNA targets

Ph. Bernhardt*, W. Friedland, P. Jacob, H.G. Paretzke

GSF—National Research Center for Environment and Health, Institute of Radiation Protection, D-85764 Neuherberg, Germany

Received 17 February 2002; accepted 10 June 2002

Abstract

To study the influence of inhomogeneous targets on radiation-induced DNA damage, photon and electron track structure calculations in the biophysical simulation code PARTRAC were carried out taking into account the different mass densities and atomic compositions of DNA, histone proteins and the cell plasma. Particularly interactions of USX rays up to 3 keV are affected by the photoionization of carbon, nitrogen, oxygen and phosphorus. Whereas the succeeding relaxation of these low Z elements does not seem to have a strong influence on the production of DNA damage, the differences between the cross-sections of DNA and cell plasma, particularly between the carbon and oxygen K absorption edge (0.29–0.54 keV), lead to a significantly local inhomogeneous dose distribution and therefore an increased yield of strand breaks per unit dose, especially when DNA is folded and proteins are attached. Resulting small fragment size distributions reflect the DNA wrapping around the histone octamer and supports an irregular crossed linker model for the chromatin fiber architecture. The evaluation of large fragment size distributions shows deviations from random breakage model, most notably in the case of C_K USX irradiation, which should be taken into account, when DSB yields are determined in experiments. (Int J Mass Spectrom 223–224 (2003) 579–597)

Keywords: Monte Carlo simulation; DNA damage; UVX irradiation; Structured target

1. Introduction

DNA has long been known as a crucial target for radiation-induced biological effects. The formation of initial damages like single strand breaks (SSBs), double strand breaks (DSBs) and base damages of various types and particularly local clustering of these lesions is presumably the first step for the development of chromosome aberrations, mutations or cell inactivations. Due to the stochastical nature of the particle track structure, Monte Carlo simulations are an adequate technique to investigate the effectiveness of different particles and initial energies, which is thought to be mainly a consequence of different energy deposition densities [1].

Photon interaction in biological matter with ultrasoft X-rays up to 10 keV is mainly photoionization, leading to the emission of photoelectrons and Auger/Coster–Kronig electrons during relaxation process. These low energy electrons deposit the main part of the initial photon energy close to the relaxed atom. The cross-sections for the photons and the electrons as

* Corresponding author. E-mail: bernhardt@gsf.de

1387-3806/02/$ – see front matter
PII S1387-3806(02)00879-5

well as the course of the relaxation cascade strongly depends on the local atomic composition and varying mass densities of the different substances in the cell nucleus, like DNA, histone proteins or plasma. Earlier track structure calculations have often neglected these effects by assuming a homogeneous medium [2–5].

Similar to Michalik and Begusova [6] and Terrissol and Vrigneaud [7], in this work the biophysical simulation code PARTRAC [4,5] was extended by taking into account structured targets for the calculation of track structures. The target models consider different degrees of DNA folding like free, linear DNA or compact chromatin fiber in a complete cell nucleus and are based on the atomic representation of [4] with the additional consideration of an atomic description of the histones by measurements of Luger et al. [8] and Ramakrishnan et al. [9]. Initial SSB and DSB yields per unit dose for the different target models are presented, together with sensitivity analysis of uncertain parameters like the effectiveness of the radical transfer mechanism in cellular environment. Furthermore, the improved model is applied to obtain fragment size distributions that are compared with new experimental data in order to obtain information about the geometric folding of DNA inside the chromatin fiber and the cell nucleus.

2. Methods

2.1. Target models

The geometry of the DNA and the histones is defined by an "atomic volume model", following the idea of Michalik and Begusova [6]. Here spheres around the constituent atoms with the corresponding van der Waals radius are united to represent the volume of the DNA and the histones; the geometry of the plasma is defined by the remaining volume. The used van der Waals radii are C: 0.17 nm, N: 0.15 nm, O: 0.14 nm, P: 0.19 nm and S: 0.18 nm [10]. Important to note is the fact, that this model is only useful to describe macromolecular geometric properties, for example the twisted helical shape, but no surface details, because molecular orbitals have mostly a non-spherical shape. It is therefore not necessary for the modeling of the geometrical shape to complete the primary atomic datasets of the X-ray crystallography measurements by the missing hydrogen atoms. Furthermore, USX photons have wavelengths in the range of the DNA diameter of 2 nm, thus their pathways are hardly influenced by target details smaller than this order of magnitude. The spheres of adjacent atoms of a molecule only overlap in the case of a chemical binding. Thus, the geometry of the investigated molecules are quite holey. Furthermore, the total volume determined by Monte Carlo integration is smaller than the expected one worked out from the total mass and the mass density. The density of DNA, histone and plasma in the cell nucleus is 1.7 [11], 1.3 [12] and 1.0 g/cm^3 [13], respectively. Therefore, a phenomenological factor s is introduced [6], scaling the van der Waals radii to get the total volume in agreement with the predicted one. For the DNA and the histone a factor of $s = 1.3$ and $s = 1.4$, respectively, is necessary. Fig. 1 demonstrates the reduction of holes by applying a scaling factor for the linear DNA (Fig. 2a). The percentage of occupation by the atomic volume model as a function of the radial distance from the axis of the double helix is shown for different values of s. For $s = 1$, only 80% at the position of the central axis ($r = 0$) is allocated, caused by the mutually unbounded bases in the stack, whereas for $s = 1.3$ no holes are left. It is difficult to detect, whether there are still some small holes for $s = 1.3$ at radii, where the grooves can already be seen ($r > 0.2$ nm).

Three different types of DNA target models have been developed and used in the simulation package PARTRAC: a piece of linear DNA, a nucleosome core particle and a piece of chromatin fiber. The linear B-DNA consists of 200 randomly chosen deoxynucleotide pairs, which atomic coordinates are based on [10] (Fig. 2a). Consecutive base pairs were calculated with a z-shift of 0.3375 nm and a helical turn of 36°.

The atomic coordinates of the core particle are taken from X-ray structure measurements of Luger et al. [8]. This structure includes an entire 146 base pairs (bp) DNA molecule which wraps around the

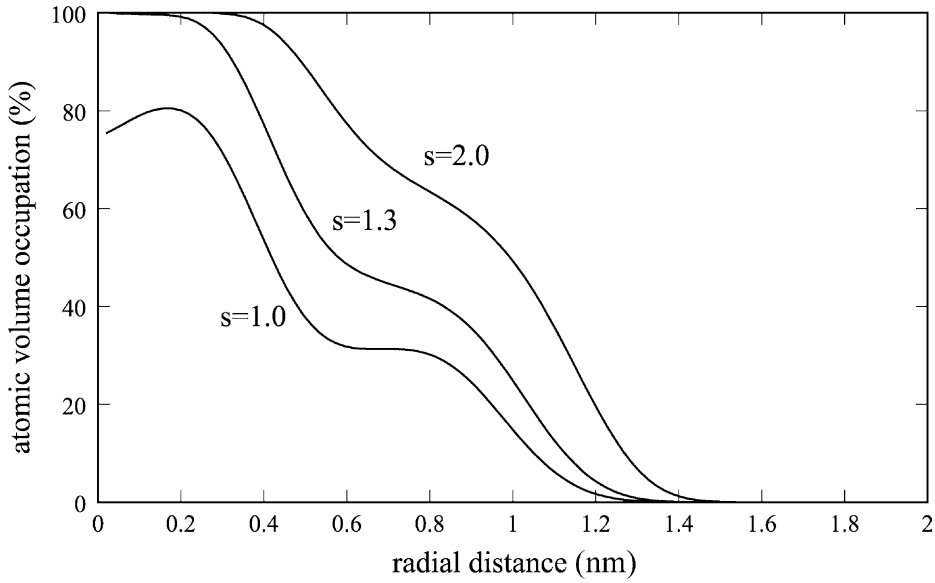

Fig. 1. Fraction of occupation by the atomic volume model in dependence on the radial distance from the central axis of the linear DNA target model. The factor *s* scales the van der Waals radii of the corresponding atoms.

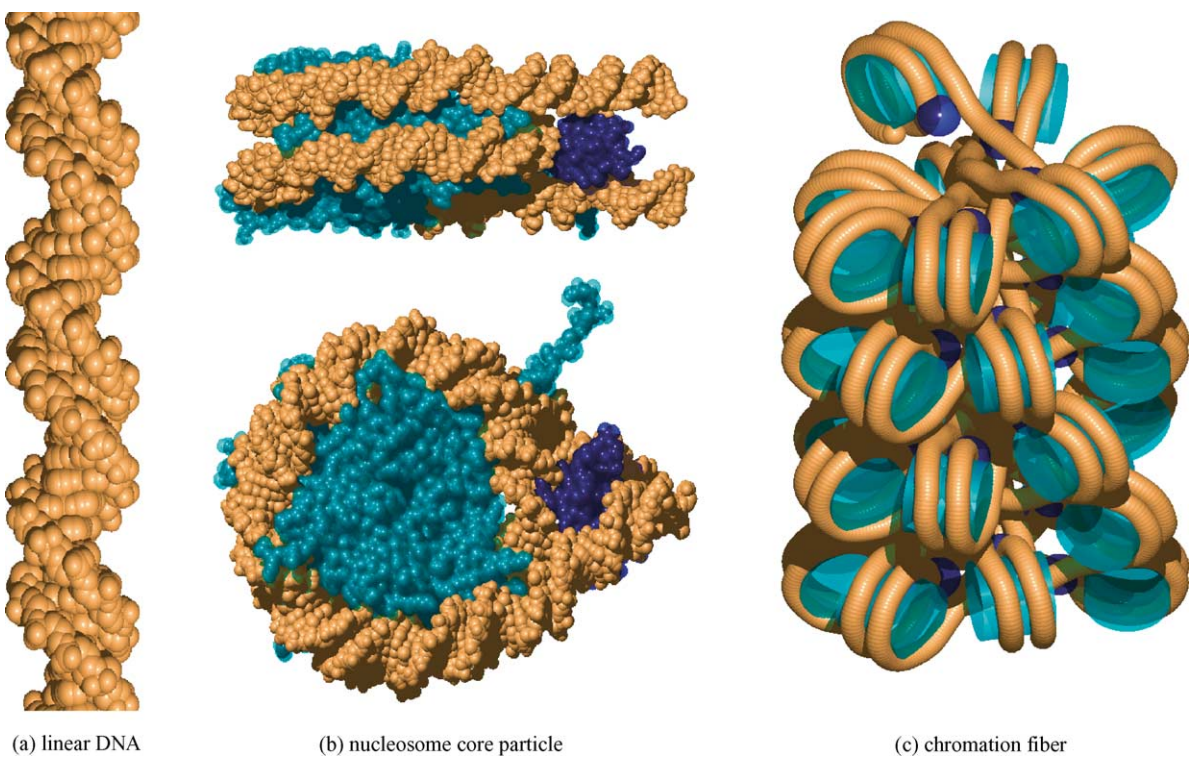

Fig. 2. DNA target models, brown: DNA helix; cyan: histone octamer; blue: globular core of the linker histone H5. The chromatin fiber target model is represented in a simplified manner to improve the visualization of the structure.

histone protein octamer with an effective number of superhelical turns of 1.65. The octamer consists of over 80% of the atomic coordinates of eight histone chains 2 × H2A, 2 × H2B, 2 × H3 and 2 × H4, including also some amino-terminal tails passing through the two parallel DNA double helices (Fig. 2b). The core particle was completed by adding a linker histone and linker DNA. For the first one the available crystal structure of the globular domain of the histone H5 [9] was used, which is a variant of the linker histone H1. The GH5 was oriented in the way that residues K69, R73 and K85 are cross-linked to the medial DNA strand in the entry-region, like it was proposed by the authors. The real position of the linker histone is still under discussion. Pruss et al. [14] proposed that the globular domain of the histone is located asymmetrically inside the gyres of the DNA, Thomas [15] located the H1 histone asymmetrically close to the dyad axis. The linker DNA segments were added in the way, that they leave the octamer immediately tangentially and continue until they reach an "intersection zone" about 8 nm away from the nucleosome center. This stem-like architectural motif requires the linker histone and can be seen with the help of electron cryomicroscopy at low ionic strength [16]. Alternatively the stem motif is build up by linker DNA segments, which conclude two complete turns around the octamer and then leave the nucleosome in parallel [17].

The organization inside the chromatin fiber is not completely understood until now. The diameter of the fiber is around 30–45 nm [18], seems to be dependent on the linker length [18], but quite independent on the ionic strength [19]. The mass per unit length at physiological ionic strength is 5.9 nucleosomes per 11 nm fiber length, measured by X-ray and neutron scattering on isolated fragments of chromatin [18,20]. The nucleosomes are located predominantly at the fiber periphery and the linker DNA tends to project towards the fiber center [21–24]. Generally two different models of chromatin folding are discussed: solenoid [25] and crossed linker models [26]. Whereas solenoid models seem to be more and more in disagreement with experimental observations [4,16,27], there are also more and more doubts about any regular arrangement of the nucleosomes [19,21]. An atomic representation of a crossed linker model with stochastic elements has been developed (Fig. 2c) in the style of [16]. Nucleosomes, together with their stem motif, are radially disposed with a distance of 11.5 nm between the fiber axes and the center of mass of the nucleosome [24], leading to a total fiber diameter of 34 nm. The consecutive nucleosomes are shifted parallel along the fiber axis with 1.9 nm leading to the above-mentioned package density. Adjacent nucleosomes are located at the opposite site of the fiber, alternate nucleosomes appear directly next to each other [22]. The DNA linker segments are connected at the "intersection zones" with smoothly bended and mutually crossed pieces of linear DNA, resulting in a mean linker DNA entry–exit angle of 34° [16]. The average linker length is 49 bp resulting in a nucleosomal repetition length of 195 bp. A direct stacking of the nucleosomes is avoided to reduce physical close distances.

2.2. Hydration shell

The hydration shell of the DNA plays an important role concerning radiation-induced damage. The degree of hydration is given as Γ in mol water per mol nucleotide. Swarts et al. [28] supposed, that the yield of the release of unaltered bases per unit dose for $\Gamma = 12$–15 is the same as that for the DNA, explaining this result by a charge transfer effect from inner tightly bounded first water shell to DNA, whereas outer, more loosely bounded water molecules of the second water shell tend to dissociate and generate hydroxyl radicals. LaVere et al. [29] and Debije et al. [30] used electron spin resonance and could not detect $OH^{\bullet}$ radicals at hydration levels of approximately $\Gamma = 9$ and $\Gamma = 9$–11, respectively, in irradiated DNA at low temperatures, also proposing a hole transfer for this hydration shell. Less is known about the mass density of the hydration shell, which could be slightly increased in comparison to liquid water due to the negative charged DNA molecule. According to Danielewicz-Ferchmin and Ferchmin [31], hydration density of single charged metal atoms do not deviate very much from normal liquid water. Thus, it

is assumed, that the hydration shell does not have a different influence on track structure than the plasma, but it has to be considered when damages are scored. To avoid again designing a too detailed target model for reasons mentioned above, the first hydration shell is modeled in PARTRAC by an additionally increased radius of the DNA atoms by a factor of 1.8 as a consequence of its mass density and the mass of the first hydration shell for $\Gamma = 10$. This leads to a thickness of the water shell of approximately 0.3 nm in agreement with typical hydrogen bonding distances [32].

2.3. Higher order structure

The three target models were put into boxes, whose dimensions provide at least a 4-nm diffusion shell around the targets to be able to simulate the radiation chemistry in cellular environment (see below). The piece of chromatin fiber was additionally used to design a complete mammalian cell nucleus with homogeneously distributed 6×10^9 bp divided into 46 chromosomes, considering chromatin fiber loops and chromosome domains. A detailed description can be found in [5]. The shape of the cell nucleus is a cylinder with radius and thickness of 5 μm.

2.4. Cross-sections

Due to the lack of cross-sections for electron interactions in DNA, histones and plasma, cross-sections for liquid water from Dingfelder et al. [33] were taken and scaled by the respective mass density, which values are mentioned above. This scaling is supported by LaVerne and Pimblott [34], who showed, that the mean energy loss per unit mass for 1 MeV incident electrons in DNA and liquid water are comparable. In Fig. 3, the resulting inelastic and total mean free path of electrons for DNA, histone and the plasma can be seen. For the photons the independent particle approximation is used. Here the cross-sections were derived from the sum of the cross-sections of the constituent atoms, neglecting molecular binding effects. Hatano [35] demonstrated, that the photon absorption cross-sections of the two isomers cyclopropane and propylene are almost the same and are equal to the sum of the cross-sections for the constituent atoms, until differences due to the molecular structure can be measured for photon energies below 16–18 eV. The atomic cross-sections are taken from [36], in which subshell binding energies seem to have small differences between more recent values, as pointed

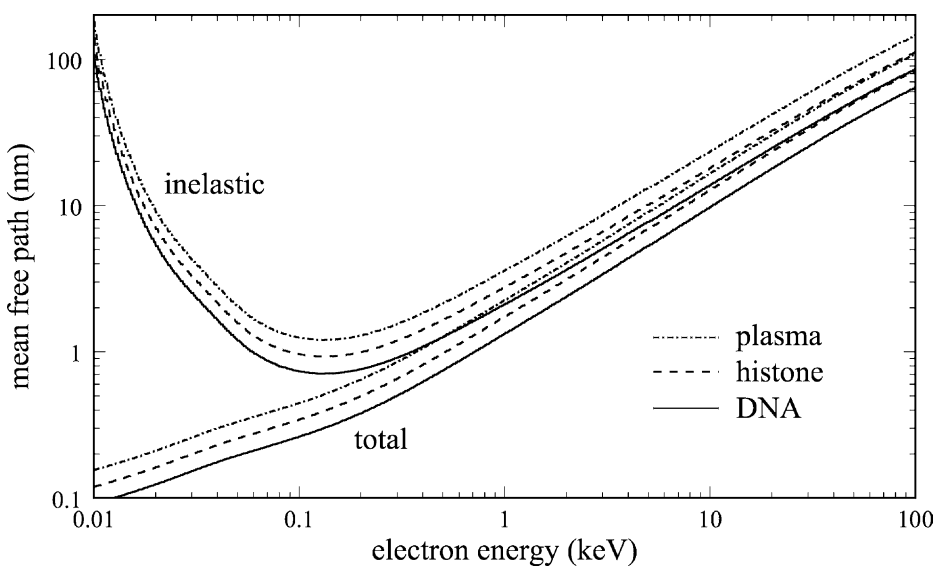

Fig. 3. Total and inelastic mean free path for electrons in liquid water, scaled by density to describe different media.

Table 1
Weight fraction of the used materials

	DNA	Histone	Plasma
Hydrogen (%)	3.7	7.8	10.6
Carbon (%)	37.9	53.0	9.0
Nitrogen (%)	17.2	19.1	3.2
Oxygen (%)	31.2	19.7	74.2
Phosphorus (%)	10.0	0.0	2.6
Sulfur (%)	0.0	0.4	0.4

The weight fractions for DNA and histones are derived from the atomic datasets together with the missing hydrogen, the values for the plasma are taken from [13].

out by the authors, but have the advantage of being consistent with the relaxation data [37]. Furthermore, the absorption fine structure near to the edges is not incorporated in the data. The used weight fractions of the plasma, DNA and histones are given in Table 1. The weight fraction for DNA and histone are derived from the atomic data sets together with the missing hydrogen, the values for the plasma in the cell nucleus is taken from [13]. Although the latter one already includes the DNA and the histones, it is a neglectable small amount in the assumed cell nucleus size of approximately 400 μm^3. Fig. 4 shows the resulting photon mean free paths for the three different materials. Remarkable are the photoionization edges at 0.14 keV (P–L2, P–L3), 0.19 keV (P–L1), 0.29 keV (C–K), 0.40 keV (N–K), 0.54 keV (O–K) and 2.13 keV (P–K). Those lead to large differences in the mean free path particularly between the C–K and O–K edge [7], due to carbon and nitrogen-rich DNA and histones.

2.5. Relaxation

Whenever photons remove inner shell electrons by photoionization the atoms relax by radiative (fluorescence) or non-radiative (Auger or Coster–Kronig) transitions. New relaxation data [37] are included in PARTRAC. The possible transitions and emitted photons and electrons are evaluated by Monte Carlo reorganization code, based on Pomplum [38] and Pomplum et al. [39], assuming unbound atoms. The holes are filled up successive from the inner to the outer shells until the valence shell is reached, whereby the transition probabilities are scaled by the fraction of the number of remaining electrons and renormalized to one, except in the valence shells, where immediate neutralization is assumed during the relaxation. The angular distribution of the emitted particles is assumed to be isotropic. The difference between the absorbed initial photon energy and the sum of all energies emitted by electrons and photons,

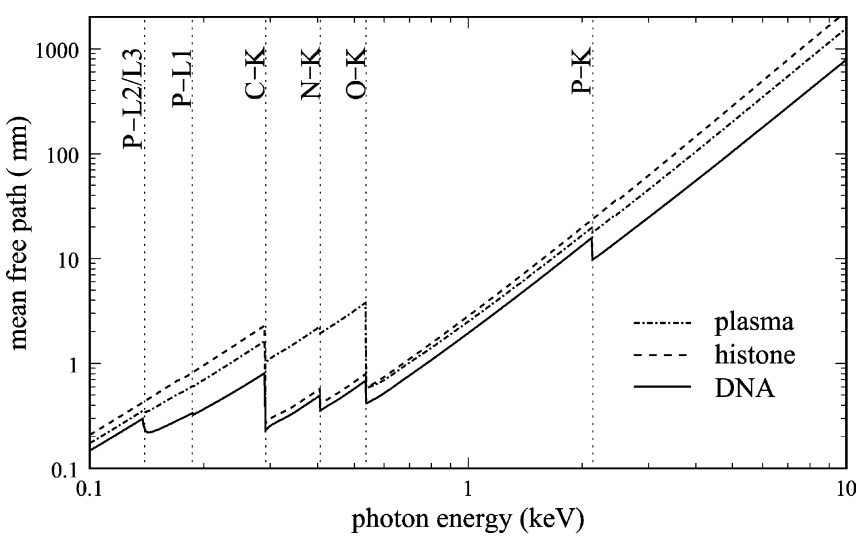

Fig. 4. Total mean free path for photons in different media.

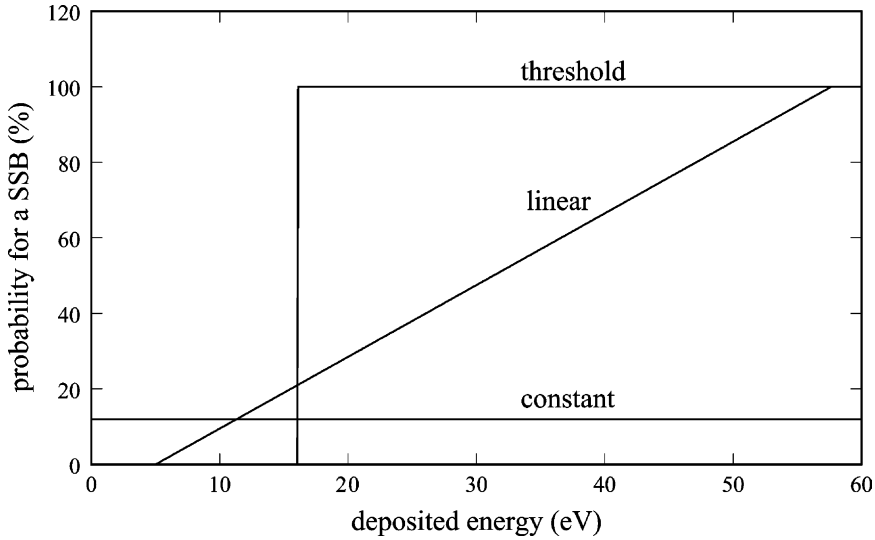

Fig. 5. Different probability functions for the production of a SSB in dependence on the deposited energy in a sugar phosphate group including the attached first hydration shell.

is scored as a local energy deposition and is a measure of the resulting charge of the relaxed atom. Shake-off processes are neglected.

2.6. Particle interaction with DNA (direct effect)

Regarding the probability of a single strand break in dependence on the direct deposited energy in one sugar phosphate group (including the attached first hydration shell), three different ways, shown in Fig. 5, have been investigated: a threshold, linear and constant dependence. The threshold model assumes a definite break, when a certain amount of energy is deposited and has often been used [2–5]. To account for experimental observations, that DNA strand breaks can also be induced by low energy electrons [40] and photons [41–43] down to 4.9 eV particles, a linear model, which has its origin at 5 eV and increases up to 100%, and a constant model, in which the occurrence of a SSB is independent on the deposited energy, have been introduced and tested. All the three models have one free parameter, which is fixed by a fit to the value of 350 SSB per Gray and cell nucleus for the direct effect in cellular environment for ^{60}Co γ-irradiation. This value is derived from the total SSB yield of approximately 1000 SSB per Gray and cell nucleus [44] and the ratio between the direct and indirect effect of 35:65 [1]. The fits lead to a threshold value of 16 eV (close to 17.5 eV, which is used by Nikjoo et al. [45]), a slope of 1.9%/eV for the linear model and a constant probability of 12% as shown in Fig. 5. As the main probability function in PARTRAC the linear model is used, because it takes into account the results of the above-mentioned experiments [40–43].

2.7. Radiation chemistry (indirect effect)

All energy depositions outside of the DNA, the first hydration shell and the histones lead to the production of water radicals. The simulation of this radiation chemistry includes the production, the diffusion and chemical reactions of the species e_{aq}^-, H_3O^+, $OH^\bullet$, $H^\bullet$ and H_2 in the time from 10^{-12} to 10^{-8} s after irradiation. A detailed description of the present simulation procedure is given in [5]. Scavenging of the $OH^\bullet$ radicals is either possible by scavengers in the solution with a capacity of $4 \times 10^8\ s^{-1}$ [46] or if such a radical moves inside the volume of the histones [47]. Whenever $OH^\bullet$ radicals react with the sugar phosphate group of the DNA, a SSB is created with a probability of 65%

as suggested by Nikjoo et al. [45]. This value is derived from the experimental observation, that the efficiency of SSB formation per $OH^{\bullet}$ radical interaction is about 13% and that the ratio between sugar phosphate and base reactions of $OH^{\bullet}$ is approximately 20:80.

2.8. DSB production

Whenever two SSB (direct or indirect) appear on opposite strands and the genomic distance is smaller than 10 bp, a double strand break is scored. The value of 10 bp is used in the majority of the DNA damage simulations [2,7,45,48].

Siddiqi and Bothe [49] proposed, that DSB can also be produced by a transfer of radical sites from one broken strand to the opposite strand and subsequent cleavage. This process occurs with a probability of $6 \pm 2\%$ for every $OH^{\bullet}$ radical mediated SSB independent of the scavenger capacity. The alternate possibility that the second strand is damaged by a secondary radical derived from a scavenger molecule seems to be very unlikely [50]. Xapsos and Pogozelski [51] listed measurements of the effectiveness of the radical transfer mechanism on plasmids, finding a probability range between 1.1 and 4.0%. This list can be extended by 0.8% [52], 0.6% [53] and 0.2% [54]. Furthermore, measurements of strand breaks with low energy photons of 7 eV [42] and 8.3 eV [41] with dry plasmid showed a ratio of DSB to SSB of 0.6 and 3%, respectively, which lead to the question, if also direct ionized or excited DNA molecules can provoke a radical transfer, for example by rapid decays of transient molecular resonances in the case of low energy electrons [40,55]. In the present work a radical transfer coefficient of 1% for direct and indirect SSB is assumed, the influence of this parameter on RBE values will be discussed.

2.9. Calculations

In the present sets of calculations, the irradiation of the linear DNA, the nucleosome core particle and the cell nucleus by monochromatic and parallel photon beam with energies between 0.1 and 10 keV is simulated. Furthermore, 220 kVp X-rays, filtered with 0.5 mm Cu plus 4 mm Al, and ^{60}Co γ-irradiation with energies of 1.17 and 1.33 MeV are considered. In order to get electron equilibrium for the high energy irradiation, particles, which leave the volume of interest, are mirrored and enter the investigated volume at the other side. Whenever the current particle is moving within an atomic sphere, cross-sections of the corresponding material (DNA, histone) are applied, alternatively cross-sections of the plasma are used. This determination of the material is very time consuming, because in the case of the chromatin fiber over 200,000 atoms must be checked for every particle interaction. To reduce calculation time the atoms are sorted into a three-dimensional cartesian grid by a preprocess. Then only the atoms inside the meshes, which are on the way of the current particle, must be verified. An analytical approach leads to a occupation density of approximately 0.4 atoms per mesh to get the best speed improvement. By applying this ‘spatial subdivision method’ the simulation time for the track structure becomes comparable to the time consuming simulation of the radiation chemistry, so the consideration of structured targets does not require a lot of additional calculation power at all.

3. Results

3.1. SSB and DSB yields

In Fig. 6a and b the yield of SSB per Gy and Gbp caused by the direct and indirect effect, respectively, is plotted for the three different target models “linear DNA”, “nucleosome core particle” and “cell nucleus” for photon irradiation from 0.1 keV up to γ-irradiation by ^{60}Co decay. At the main edges initial energies above and beyond have been tested. The yield of direct SSB stays quite constant and independent of the used model. Exceptions are the small step at the P–L2/L3 absorption edge for all models and differentiation between the models in the energy interval between C–K and O–K. A significant change at the P–K edge is not detectable.

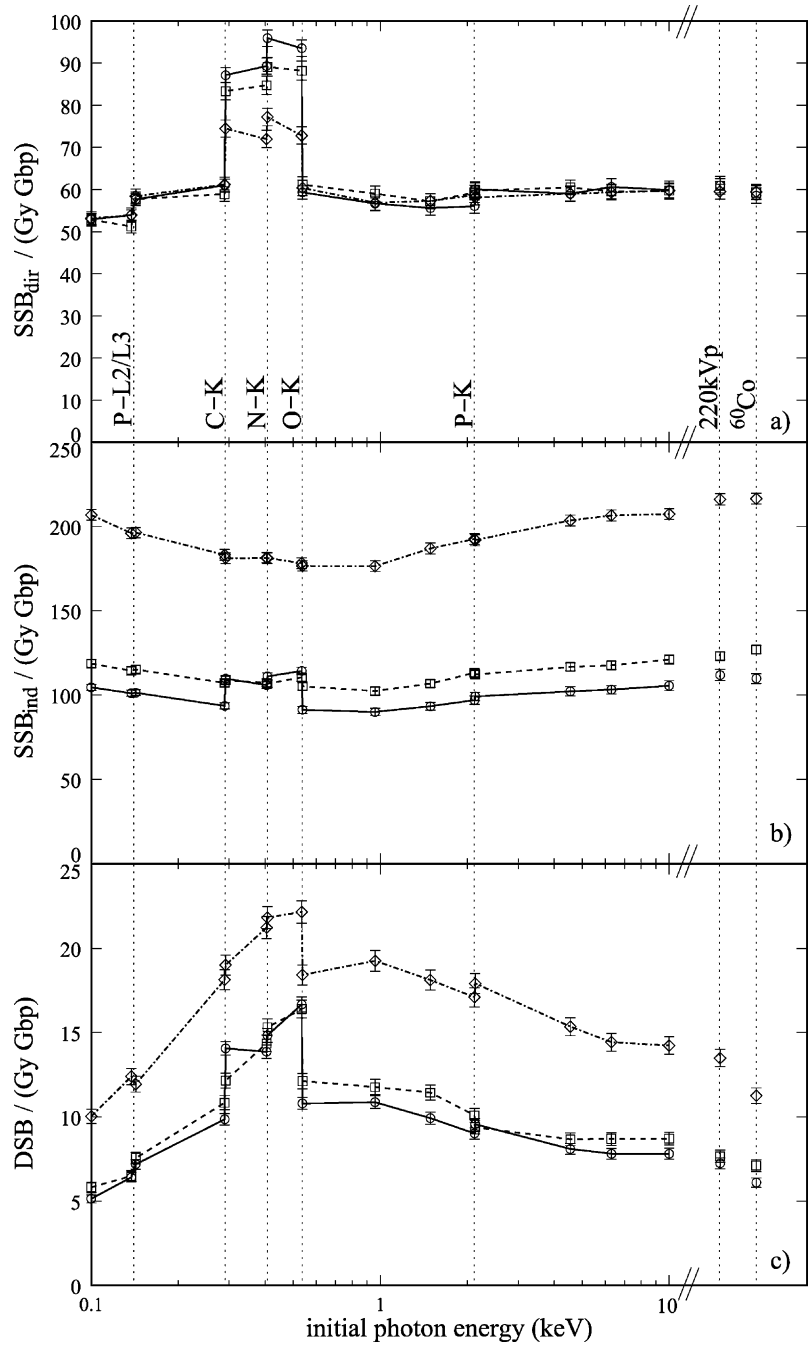

Fig. 6. Yields of direct and indirect SSB and total DSB per Gy and Gbp for different target models. Diamond, dashed-dotted: linear DNA; square, dashed: nucleosome core particle; circle, solid: cell nucleus.

Indirect effects are strongly dependent on the used model. If DNA is more and more folded, SSB yield goes down, particularly when DNA is wrapped around the histone. All curves have a slight minimum around 1 keV. Again a gain of the SSB yield in the C–K/O–K interval particularly for the more folded targets is visible. In the case of the whole cell nucleus the ratio between the direct and indirect effect for γ-irradiation is 35:65, which is in agreement with Ward [1].

Fig. 6c shows the resulting total DSB yield. Firstly, folded structures provide less DSB lesions. Secondly, a maximum of DSB production is around 1 keV beside the already observed gain in the C–K/O–K interval. Here, again, the relative increase is larger in the case of folded structures. Thirdly, there are no significant changes at P–L2/L3 and P–K edges. The absolute values for the yield of DSB per Gy and Gbp are given in Table 2, together with corresponding RBE values in comparison to ^{60}Co γ-irradiation from the simulation and from experiments. The RBE values agree with the experimental data for Ti_K and Al_K USX, whereas C_K and Cu_L USX rays have a higher yield in the experiments than predicted by the model.

Table 2
DSB yield and RBE DSB value of the simulation using the cell nucleus model and from experiments for different characteristic photon irradiation

Photon energy	DSB/ (Gy Gbp)	RBE DSB	RBE DSB (experimental data)
C_K (0.28 keV)	9.9	1.6	2.1[a] (57)
			2.7[b] (57)
			3.8[c] (71)
N_K (0.39 keV)	13.8	2.3	–
O_K (0.52 keV)	16.7	2.7	–
Cu_L (0.96 keV)	10.9	1.8	2.3[b] (57)
Al_K (1.49 keV)	9.9	1.6	1.6[d,e] (70)
			1.7[a] (57)
			1.9[b] (57)
			2.2[c] (71)
Ti_K (4.55 keV)	8.1	1.3	1.4[b] (57)
220 kVp	7.2	1.2	–
^{60}Co	6.1	1.0	–

[a] PFGE, fragment analysis.
[b] PFGE, FAR analysis.
[c] Sedimentation technique.
[d] Filter elution.
[e] Reference irradiation 250 kVp.

3.2. Sensitivity analysis

The influence of the different strand break probability models on the production of direct SSB per Gy and Gbp for the cell nucleus target can be seen in Fig. 7. Due to the fitting, the SSB yield coincide, when ^{60}Co γ-irradiation is used. For photons with smaller initial energies the differences between the three models are not very significant, only in the USX range small deviations can be seen. In the interval between the C–K and O–K edge, the threshold model leads to the highest SSB yield, whereas SSB yield above and beyond this interval is slightly increased for the constant and linear model. These small deviations also appear in the case of the linear and the nucleosome target model, as well as for the production of DSB in general (results not shown).

Different effectiveness of the radical transfer mechanism ranging from 0 to 3% are tested in Fig. 8. The more the radical transfer mechanism dominates, the more the relative yield of DSB per Gy and Gbp gets less dependent on the initial particle energy. In the case of 0% C_K USX rays have an increased RBE DSB value of 1.9 in comparison to ^{60}Co γ-irradiation, whereas 3% decreases the RBE DSB value to 1.4.

3.3. Fragment size distribution

Fig. 9 illustrates the number of small single stranded fragments in a range between 50 and 150 bp in the case of X-ray irradiation of the whole cell nucleus with 80 Gy. Beside the number of total fragments, the production of fragments due to the direct and indirect effect can be seen. Furthermore, a scan of Fig. 5a of [27] is given on the right upper corner, which shows the fragment distribution resulting from measurements on GM38 cells, irradiated with the same dose and radiation type. In both plots, a significant peak can be seen at 78 bp having a similar shape, but being a little bit broader in the case of the experiment. In the simulation this main maximum is accompanied by smaller peaks, which are more difficult to localize; a rough estimation yields maxima at approximately 64, 73 and 92 bp, whereas in [27] smaller peaks are found

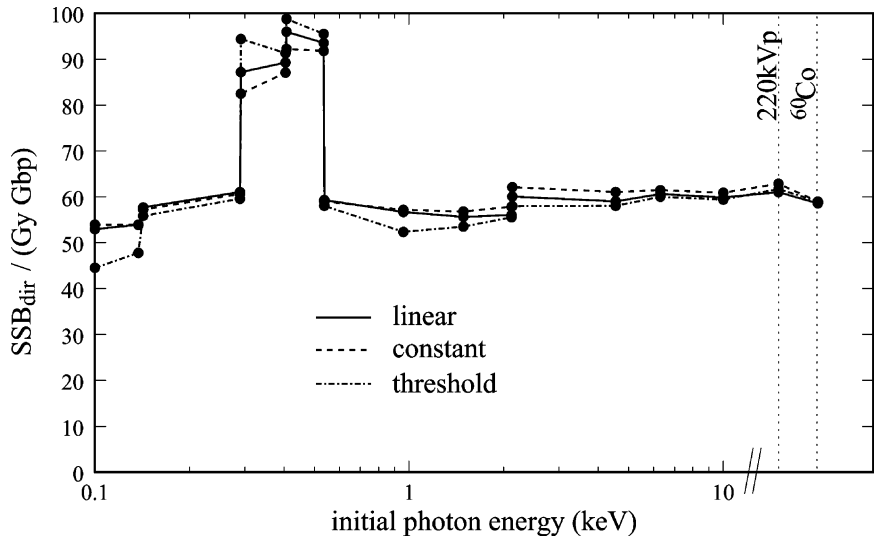

Fig. 7. Direct SSB yield per Gy and Gbp for different strand break probability functions for the cell nucleus target model.

at 68 and 88 bp, a further might be visible at 62 bp. The SSB fragments due to the direct effect have a clear maximum at 77 bp, in the case of the indirect effect peaks are at 62, 73, 82 and 93 bp.

The number of larger fragments in the range of 0–2000 bp is plotted in Fig. 10 in arbitrary units, using the same parameters as in Fig. 9. Fig. 2a of experimental results in [27] is printed in the right upper corner. In the simulation beside the already discussed prominent peak at around 78 bp a maximum is visible at 195 bp, two larger peaks at 304 and 378 bp and then a large number of broad and small peaks up to

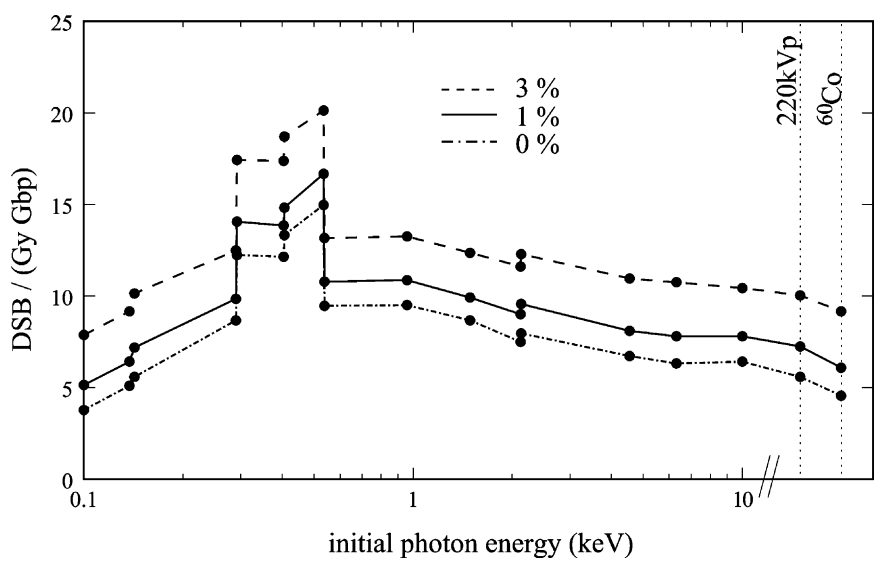

Fig. 8. Total DSB yield per Gy and Gbp for different effectiveness of the radical transfer mechanism for the cell nucleus target model.

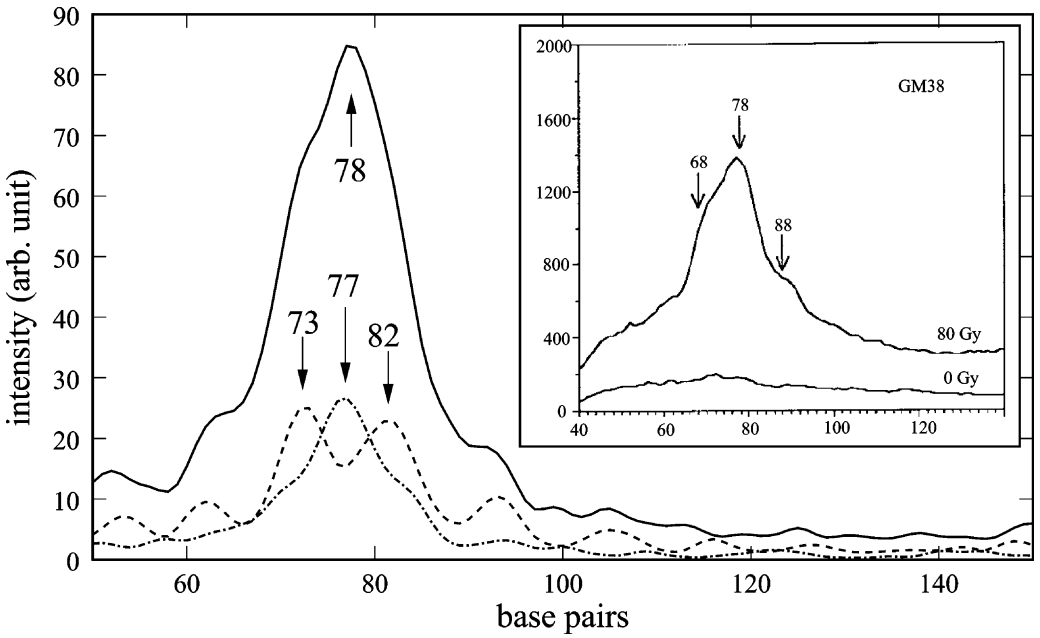

Fig. 9. Number of small SSB fragments between 50 and 150 bp in arbitrary units due to 220 kVp irradiation and 80 Gy in the case of the cell nucleus target model. Solid: total number of SSB fragments; dashed-dotted: SSB fragments due to the direct effect; dashed: SSB fragments due to the indirect effect. In the right upper corner is a scan of Fig. 5 of [27], showing the measured total number of SSB fragments for X-rays irradiation at 0 and 80 Gy in arbitrary units.

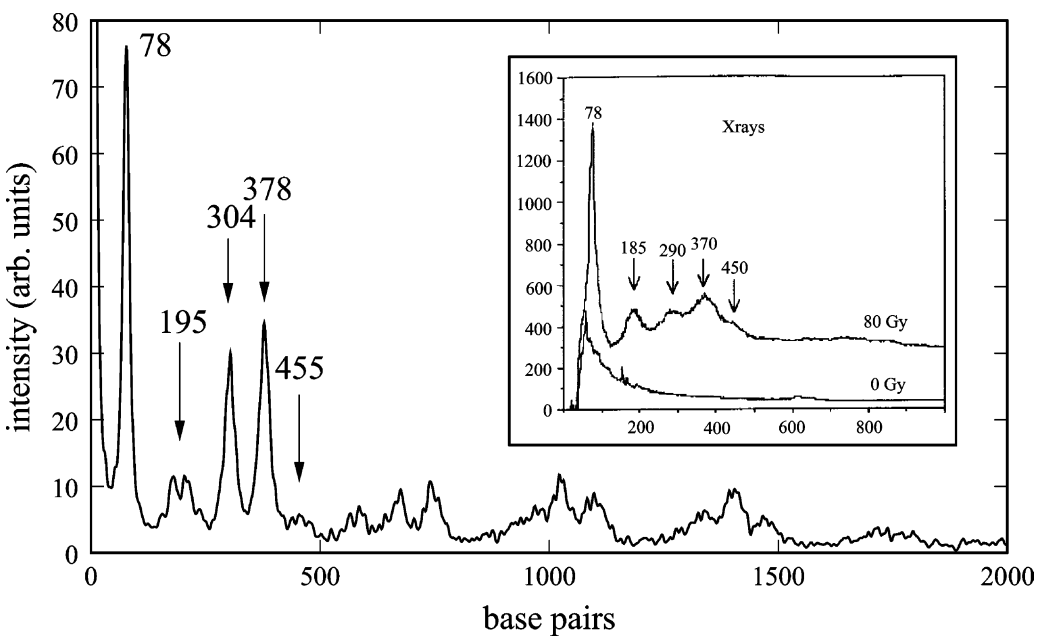

Fig. 10. Number of total SSB fragments between 0 and 2000 bp in arbitrary units due to 220 kVp irradiation and 80 Gy in the case of the cell nucleus target model. In the right upper corner is a scan of Fig. 2a of [27], showing the measured total number of SSB fragments for X-rays irradiation at 0 and 80 Gy in arbitrary units.

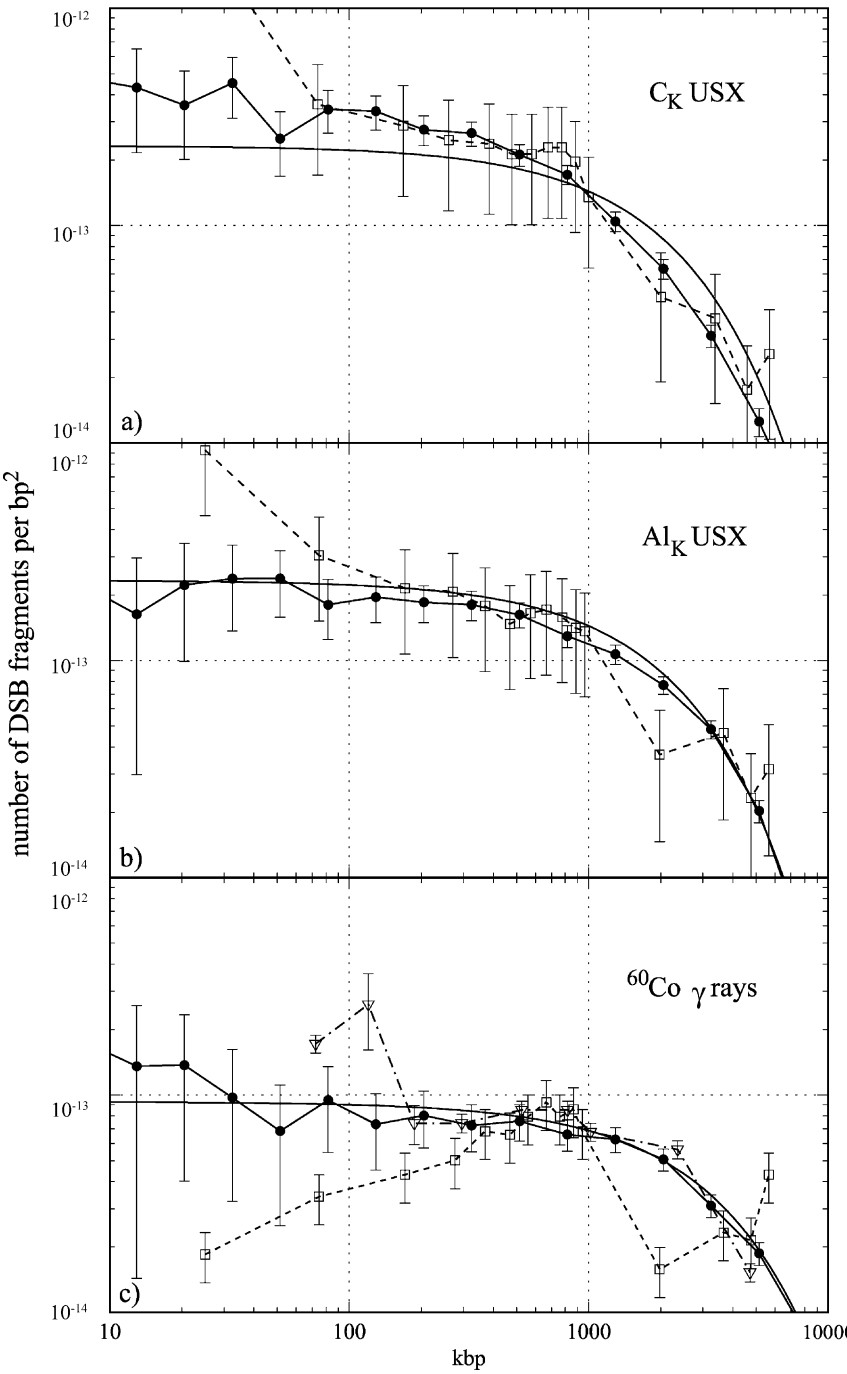

Fig. 11. Frequency of DSB fragments per bp^2 for DNA irradiated with photons of different energies. Filled circle, solid: simulation results; solid: expected distribution according to [56] in the case of a random breakage; squares, dashed: measurements of deLara et al. [57]; triangle, dashed-dotted: measurements of Höglund et al. [58].

2000 bp. Rydberg et al. [27] found broad and weak maxima at 185, 290, 370 and 450 bp and then a flat distribution up to 1000 bp.

Finally Fig. 11 gives the frequencies of large DSB fragments per bp squared in the range between 10 and 10,000 kbp for three different types of irradiation at a dose of 50 Gy. Beside the results from simulations the corresponding distributions in the case of a random breakage according to [56] are shown. Furthermore, experimental data with the same dose and irradiation type from deLara et al. [57] (rectangles) with V79-4 cells and from Höglund et al. [58] (triangles) with human fibroblast cells are plotted. ^{60}Co γ and Al_K USX rays generate fragment distribution in agreement with the randomly broken stick model [56] in that range with slightly reduced values on average. C_K USX rays in contrast produce significantly a non random distribution [5]. Below 1000 kbp the number of fragments is increased, whereas larger fragments up to 10,000 kbp are generated more seldom.

In comparison to the experimental data there is quite good agreement above approximately 200 kbp fragment size. For smaller fragment sizes experimental data show a more or less increased yield in comparison with the randomly broken stick model for different photon energies like Höglund et al. [58], Newman et al. [59] and Löbrich et al. [60] with exception of deLara et al. [57] who found for ^{60}Co γ-irradiation a decreasing number of small fragments. In the case of the simulation a significant change in behavior for small fragments can not be detected, which might be due to more compact chromatin fiber loops in reality than now modeled in PARTRAC.

4. Discussion

4.1. SSB and DSB yields

According to Fig. 6 the production of SSB due to direct effects seems to be only dependent on the received local dose and independent on different ionization densities within one track and the folding of the DNA, since it is quite constant in a large energy range above the O–K edge for different target models. Whenever total photon cross-sections between DNA and the surrounding medium differs, the local dose should change with the same efficiency. If, however, the range of the secondary electrons is very large, they transport the energy far away from the point of production, ending again in a homogeneous dose distribution. This happens at the P–K edge, where a sudden increase to a ratio 1.9 between the photon cross-sections of DNA and plasma does not affect significantly the SSB yields in all target models, because of a long range of the secondary electrons of approximately 150 nm in comparison to the DNA diameter. In contrast, in the energy interval between the P–L2/L3 and the O–K edge, where cross-sections distinguish up to a factor of 5.5 near the O–K edge, inhomogeneous dose distribution occurs. Additionally, the folding of the DNA and the adding of carbon- and nitrogen-rich histones allows additional damage through secondary electrons from photoionized neighbored molecules.

The indirect effect is dependent on the accessibility of the DNA. Hence, folded DNA together with the bound histones protect from damages. The reduction of around 50% between the linear DNA and the nucleosome core particle reflects that about one-half of the DNA's surface is bound to the proteins. The further reduction of the number of SSB in the chromatin fiber is quite small in agreement with simulations in [61], because the diffusion length of water radicals of 4 nm [3,62] at cellular scavenging capacity is small in comparison with the typical nucleosome size of 11 nm. Nygren et al. [52] in contrast observed much higher protection effects of proteins and DNA folding for SSB production of a factor of approximately 100. This high yield is probably a consequence of a reduced scavenger capacity due to preparation methods [63]. The slight minimum around 1 keV for all models is a result of the high ionization density at that energy. Photons with 1 keV energy mainly ionize the K shell of oxygen, generating a photo and Auger electron with energies around 0.5 keV. These electrons produce enough radicals within a small volume, particularly if the two tracks overlap, hence, intratrack radical–radical recombination is increased. Fulford

et al. [64] measured a much stronger minimum at 1–2 keV. However, this experiment was done at low scavenging capacity, where the diffusion length of the radicals is larger and therefore radical–radical recombination becomes the dominant process. Again the influence of the inhomogeneous dose distribution is visible, particularly between the C–K and O–K edge in the case of the cell nucleus target model.

The occurrence of a local maximum at about 1 keV in the DSB yield is caused by the relative high ionization density at that energy as mentioned above, leading to many DSB from the direct effect. Thus, high ionization density results in lower indirect SSB yield but higher direct DSB yield in agreement with [7]. The gain in the C–K/O–K interval is, again, due to inhomogeneous dose distribution. At the P–L2/L3 edge the total energy is too small to produce sufficient DSB to profit from the inhomogeneity of the dose, whereas at the P–K edge there is no significant inhomogeneous dose distribution any more, as mentioned above. The after inner shell ionization relaxed and therefore highly charged low Z atoms like C, N, O and P do not significantly increase the number of DSB in the simulation in agreement with experimental results [65,66]. The qualitative shape of the DSB curve is in agreement with the simulations of Terrissol and Vrigneaud [7] for linear DNA. They used pure water as the surrounding medium, resulting in a bigger difference between the cross-sections, leading to sharper steps at the C–K, N–K and O–K edges. The absolute value of 6.1 DSB/(Gy Gbp) for ^{60}Co γ-irradiation with the cell nucleus target model is comparable with experimental data ranging from 2.8 to 10.7 DSB/(Gy Gbp) [67], using different measurement techniques and cell lines. To avoid the influence of these factors it is more convenient to compare only the RBE DSB values with reference to ^{60}Co γ-irradiation. The large differences of the present work and experimental results for the RBE values for C_K and Cu_L USX rays could be a consequence of the small mean free path of 1.6 and 2.2 μm in plasma, respectively, in comparison with the cell thickness of 5 μm, leading to a global inhomogeneous dose distribution. Then on one hand possible heterogeneous target distributions become important, which is postulated by Cole et al. [68], on the other hand fragment distributions could become nonrandom, leading to overestimation of the effectiveness of such USX rays in experimental determinations (see below).

In summary, the consideration of inhomogeneous targets leads to an increased SSB and DSB yield per unit dose in the C–K/O–K energy interval, particularly, when DNA is folded and proteins are added.

4.2. Sensitivity analysis

The small influence of the shape of the probability function on the direct SSB yield in Fig. 7 reflects that the distribution of the electron's energy deposition is quite independent on the initial energy. Only when electron energy becomes very low, mean deposited energy slightly decrease, which leads to lower yields in the case of the threshold model. In the energy interval between the C–K and O–K, in contrast, the threshold model leads to the largest SSB yields. This is caused by the direct energy deposition of the photons during photoionization, frequently occurring at the K shell of carbon and nitrogen in the DNA in that energy interval due to the large difference of the cross-sections of DNA and plasma. These direct energy depositions amounts at least 20 eV, hence the threshold model will count these as breaks, whereas the linear and particularly the constant model score these events with lower probability. In summary it is not possible to verify or rule out any of the tested probability function, because resulting SSB yields do not differ very much.

In contrast, the radical transfer mechanism coefficient can change the DSB yield result very much. Due to a quite constant level of the direct and indirect SSB yield, a high swing over effect provides an energy independent DSB value for all photon energies, which flattens the DSB yields in disagreement with the experimental results. Ward et al. [69] treated mammalian cells with hydrogen peroxide. At a concentration of 5×10^{-5} M 10,000 SSB per cell have been measured, which corresponds to a equivalent dose of 10 Gy for low LET radiation [44]. In the case of the hydrogen peroxide no significant reduction of cell survival fraction has been seen, whereas irradiation

at that dose is lethal [70]. Assuming that DSB are an important molecular lesion leading to cell death [57,71], the radical transfer mechanism coefficient might be even lower than 1% in cellular environment.

4.3. Fragment size distribution

The prominent peak in the SSB fragment distribution in Fig. 9 is a consequence of the close contact of the two DNA helices on the surface of the histone octamer, where around 80 bp complete one turn. To explain the details of the peak, Fig. 12a shows the back side of core particle. Breaks due to the direct effect are expected to occur with the same probability. Thus, the number of SSB fragments is maximal, whenever a strand gets in close contact with itself. Due to the DNA winding the closest distance appears at 77 bp, leading to a single peak in the case for direct damage. The indirect effect is additionally influenced by protection effects of the histone octamer. Therefore, the fragment size distribution for the indirect effect has a 10.2 bp modulation, resulting from the winding frequency of bound DNA [8]. The arrows in Fig. 12a point out, where the main fragment size peaks are produced. The total SSB fragment distribution caused by the direct and indirect effect and combinations of both lead to a

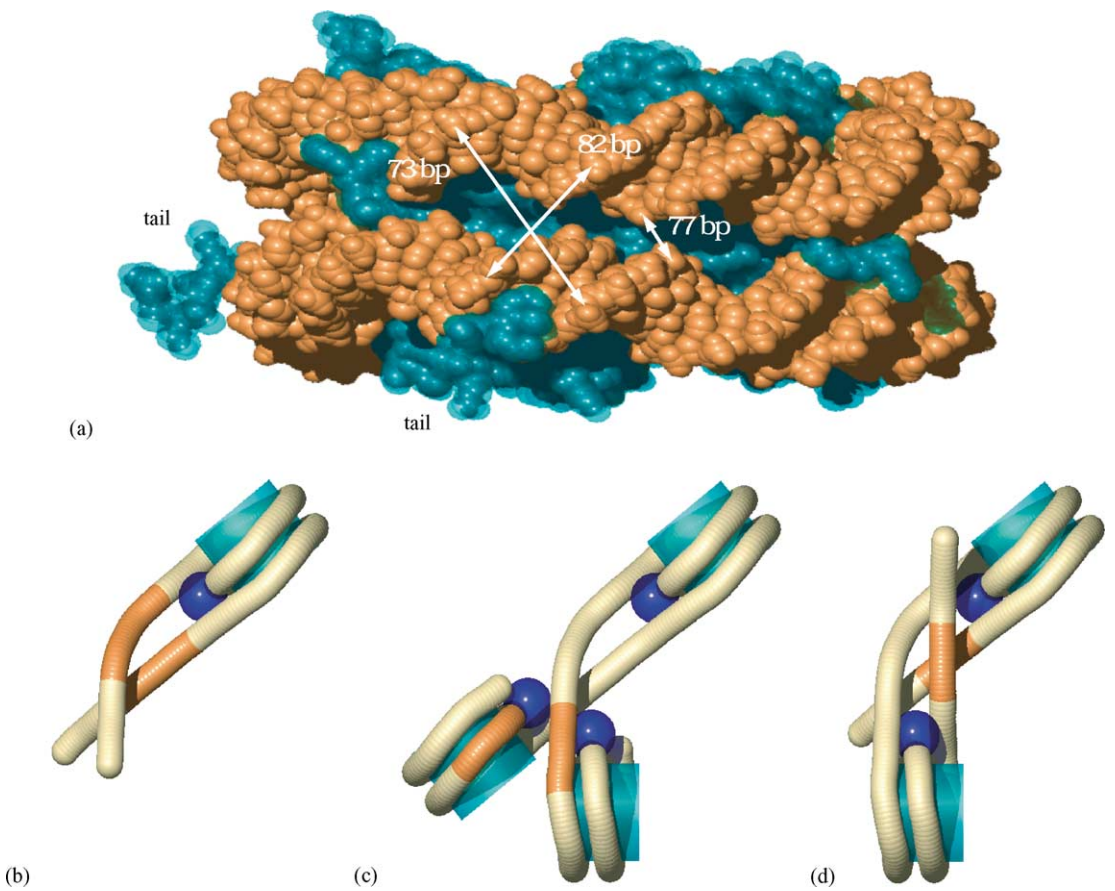

Fig. 12. (a) Back side view of the nucleosome core particle. Brown: DNA helix; cyan: histone octamer. The white arrows give examples, where the SSB fragment size of a length of 73, 77 and 82 bp are predominantly generated. (b–d) Clip of the DNA folding inside the chromatin fiber. The brown colored parts of the DNA helix indicate the positions, where the SSB fragments of 195 bp (b), 304 bp (c) and 378 bp (d) are mainly produced.

central peak with a soft shoulder on the left side and two exaltations at the bottom of the peak in agreement with experimental results. However, the 10.2 bp modulation has not a maximum at 78 bp in the simulation, which may depend on the precise phase and supercoiling of the DNA on the surface of the nucleosome [27], beside the fact, that it is difficult to determine the exact position of the smaller peaks. Further, charge migration inside the DNA and charge transfer effects from ionized histones to the DNA could result in a displacement of damage of the DNA and broadening the peak, which is not yet considered in PARTRAC.

The explanations for the three frequent larger SSB fragments 195, 304 and 378 bp is given in Fig. 12b–d. A total of 195 bp corresponds to one nucleosomal repetition length and is produced inside and next to the "intersection zone", where linker DNA mutually is crossed (Fig. 12b). Next to the entry–exit region DNA helices closely pass (Fig. 12c), which have an average genomic distance of 304 bp (≈1.6× repetition length). Finally linker DNA is crossed after running through two nucleosomes, resulting in an average fragment size of 378 bp or ≈1.9× repetition length (Fig. 12d). Together with a small peak at 455 bp, the peak pattern agrees quite well with the experimental data considering that the average repetition length in the experiment was only 185 bp. However, simulation peaks are higher and more narrow, indicating that (i) maybe the DNA strands have not a such close contact in the above mentioned regions or (ii) the Fig. 12b–d describes only preferred constellations or (iii) the linker length has a higher variation in length. The peaks above 500 bp in the simulation are mainly a consequence of the close contact of different nucleosomal layers inside the chromatin fiber. The disagreement to the measured data could have following reasons: (i) in the measurement the resolution for such large fragments is maybe not good enough to resolve the structural patterns, (ii) there is no correlation between different nucleosomal layers inside the fiber, which should lead to an increased fiber diameter to accommodate still 5.9 nucleosomes per 11 nm [4] and therefore larger DNA linker lengths is necessary and (iii) in cells in vivo the packing ratio is at least partially lowered to expand the chromatin fiber to a zig–zig structure and allow kinks and U-turns [19,21].

In summary, there is a qualitative agreement between simulation and experiment below 500 bp, indicating some kind of regularity in the region of three successive nucleosomes favoring a crossing of the linker DNA in disagreement with solenoid models.

In the case of large DSB fragments beyond 10 kbp in Fig. 11 structural patterns due to chromatin folding can not be seen in the simulation. Al_K USX rays (mean free path of 7.4 μm in plasma) and particularly γ-irradiation generate a nearly homogeneous dose distribution inside the 5-μm thick cell nucleus. Thus, deviations from random breakage model are caused by the increased yield of small DSB fragments up to 3 kbp, where Al_K USX rays are even more efficient than γ-irradiation [5]. This could lead to a small underestimation, when DSB yield is determined via fragment analysis in that fragment size interval [67]. C_K USX photons, in contrast, irradiate mainly the first layer of the cell nucleus, which produces small DSB fragments above average in the chromosomes on that side. Nevertheless, the distribution looks still quite randomly, thus a fit with the random breakage model in that fragment size interval can lead to an overestimation of effectiveness of C_K USX rays in generating DSB. This is also valid for data obtained by the simpler FAR analysis (results not shown). Important to note is the fact that the possible overestimation caused by an inhomogeneous dose distribution is strongly dependent on the thickness of the irradiated cell nucleus.

5. Conclusions and further prospects

In this work DNA damage modeling in the biophysical code PARTRAC is improved by applying structured targets for photon and electron irradiation. This leads mainly to an increased DNA DSB yield per unit dose between the C–K (0.29 keV) and O–K (0.54 keV) edge, due to a local inhomogeneous dose distribution. This gain is more pronounced, when DNA is folded and proteins-like histones are attached.

Preferable improvements of the model would be the integration of real DNA electron cross-sections and a detailed simulation of the way from the excited or ionized molecules via charge migration to the formation of measurable molecular DNA damage like strand breaks or base damages; preferable experimental data would be measurements of radiation-induced strand breaks in cells over the whole photon spectrum from the USX to the γ range, particularly observing the effects of the absorption edges P–L, C–K, N–K, O–K and P–K.

Acknowledgements

We thank Prof. Dr. C. von Sonntag and Dr. M. Dingfelder for helpful discussions. This work is supported by the European Community under Contract No. FIGH-CT1999-00005.

References

[1] J.F. Ward, Radiat. Res. 104 (1985) S103.
[2] V.V. Moiseenko, R.N. Hamm, A.J. Waker, W.V. Prestwich, Int. J. Radiat. Biol. 74 (1998) 533.
[3] H. Nikjoo, P. O'Neill, M. Terrissol, D.T. Goodhead, Radiat. Environ. Biophys. 38 (1999) 31.
[4] W. Friedland, P. Jacob, H.G. Paretzke, T. Stork, Radiat. Res. 150 (1998) 170.
[5] W. Friedland, P. Jacob, H.P. Paretzke, M. Merzagora, A. Ottolenghi, Radiat. Environ. Biophys. 38 (1999) 39.
[6] V. Michalik, M. Begusova, Int. J. Radiat. Biol. 66 (1994) 267.
[7] M. Terrissol, J.M. Vrigneaud, Proceedings of Lisbon MC2000 Conference, Springer-Verlag, 2001, p. 279.
[8] K. Luger, A.W. Mäder, R.K. Richmond, D.F. Sargent, T.J. Richmond, Nature 389 (1997) 251.
[9] V. Ramakrishnan, J.T. Finch, V. Graziano, P.L. Lee, R.M. Sweet, Nature 362 (1993) 219.
[10] R. Chandrasekaran, S. Arnott, in: W. Saenger (Ed.), Landolt-Börnstein, Numerical Data and Functional Relationship in Science and Technology, New Series VII, 1b, Springer-Verlag, New York, 1989, p. 31.
[11] D. Freifelder, Molecular Biology, Jones and Bartlett, Boston, 1987.
[12] K.T. Greulich, J. Ausio, H. Eisenberg, J. Mol. Biol. 186 (1985) 167.
[13] ICRU, Tissue Substitutes in Radiation Dosimetry and Measurement, Report 44, International Commission on Radiation Units and Measurements, Bethedsa, MD, 1989.
[14] D. Pruss, B. Bartholomew, J. Persinger, J. Hayes, G. Arents, E.N. Moudrianakis, A.P. Wolffe, Science 274 (1996) 614.
[15] J.O. Thomas, Cur. Opin. Cell Biol. 11 (1999) 312.
[16] J. Bednar, R.A. Horowitz, S.A. Grigoryev, L.M. Carruthers, J.C. Hansen, A.J. Koster, C.L. Woodcock, Proc. Natl. Acad. Sci. U.S.A. 95 (1998) 14173.
[17] C.L. Woodcock, R.A. Horowitz, Methods: a companion to methods in enzymology 12 (1997) 84.
[18] S.P. Williams, J.P. Langmore, Biophys. J. 59 (1991) 606.
[19] J. Zlatanova, S.H. Leuba, K. van Holde, Biophys. J. 74 (1998) 2554.
[20] S.E. Gerchman, V. Ramakrishnan, Proc. Natl. Acad. Sci. U.S.A. 84 (1987) 7802.
[21] R.A. Horowitz, D.A. Agard, J.W. Sedat, C.L. Woodcock, J. Cell Biol. 125 (1994) 1.
[22] D.Z. Staynov, Nucl. Acids Res. 28 (2000) 3092.
[23] A. Bernudez, S. Bartolome, J.R. Daban, J. Cell. Sci. 111 (1998) 1707.
[24] V. Graziano, S.E. Gerchman, D.K. Schneider, V. Ramakrishnan, Nature 368 (1994) 351.
[25] J.T. Finch, A. Klug, Proc. Natl. Acad. Sci. U.S.A. 73 (1976) 1897.
[26] J. Widom, Annu. Rev. Biophys. Biophys. Chem. 18 (1989) 365.
[27] B. Rydberg, W.R. Holley, I.S. Mian, A. Chatterjee, J. Mol. Biol. 284 (1998) 71.
[28] S.G. Swarts, M.D. Sevilla, D. Becker, C.J. Tokar, K.T. Wheeler, Radiat. Res. 129 (1992) 333.
[29] T. LaVere, D. Becker, M.D. Sevilla, Radiat. Res. 145 (1996) 673.
[30] M.G. Debije, M.D. Strickler, W.A. Bernhard, Radiat. Res. 154 (2000) 163.
[31] I. Danielewicz-Ferchmin, A.R. Ferchmin, Physica B 245 (1998) 34.
[32] W. Saenger, Annu. Rev. Biophys. Biophys. Chem. 16 (1987) 93.
[33] M. Dingfelder, D. Hantke, M. Inokuti, H.G. Paretzke, Radiat. Phys. Chem. 53 (1998) 1.
[34] J.A. LaVerne, S.M. Pimblott, Radiat. Res. 141 (1995) 208.
[35] Y. Hatano, Radiat. Environ. Biophys. 38 (1999) 239.
[36] D.E. Cullen, J.H. Hubbel, L. Kissel, EPDL97 The Evaluated Data Library, '97 Version, Lawrence Livermore National Laboratory, UCRL-ID-50400, 6, 1997.
[37] S.T. Perkins, D.E. Cullen, M.H. Chen, J.H. Hubbel, J. Rathkopf, J. Scofield, Lawrence Livermore National Laboratory, UCRL-50400 30, 1991.
[38] E. Pomplum, Acta Oncologica 39 (2000) 673.
[39] E. Pomplum, J. Booz, D.E. Charlton, Radiat. Res. 111 (1987) 533.
[40] B. Boudaiffa, P. Cloutier, D. Hunting, M.A. Huels, L. Sanche, Science 287 (2000) 1658.
[41] K.M. Prise, M. Folkard, B.D. Michael, B. Vojnovic, B. Brocklehurst, A. Hopkirk, I.H. Munro, Int. J. Radiat. Biol. 76 (2000) 881.
[42] K. Hieda, Int. J. Radiat. Biol. 66 (1994) 561.
[43] W. Sontag, H. Dertinger, Int. J. Radiat. Biol. 27 (1975) 543.
[44] P.J. Tofilon, D.F. Deen, Radiat. Res. 97 (1984) 171.
[45] H. Nikjoo, P. O'Neill, D.T. Goodhead, M. Terrissol, Int. J. Radiat. Biol. 71 (1997) 467.

[46] J.F. Ward, J.R. Milligan, R.C. Fahey, Factors controlling the radiosensivity of cellular DNA, in: D.T. Goodhead, P. O'Neill, H.G. Menzel (Eds.), Microdosimetry—an Interdisciplinary Approach, The Royal Society of Chemistry, Cambridge, 1997, p. 57.
[47] C. von Sonntag, The Chemical Basis of Radiation Biology, Taylor & Francis, London, 1987.
[48] V. Michalik, D. Frankenberg, Radiat. Environ. Biophys. 35 (1996) 163.
[49] M.A. Siddiqi, E. Bothe, Radiat. Res. 112 (1987) 449.
[50] R.E. Krisch, M.B. Flick, C.N. Trumbore, Radiat. Res. 126 (1991) 251.
[51] M.A. Xapsos, W.K. Pogozelski, Radiat. Res. 146 (1996) 668.
[52] J. Nygren, M. Ljungman, G. Ahnström, Int. J. Radiat. Biol. 68 (1995) 11.
[53] C. Shao, M. Saito, Z. Yu, Radiat. Environ. Biophys. 38 (1999) 105.
[54] C. Shao, Z. Yu, M. Saito, Radiat. Environ. Biophys. 39 (2000) 121.
[55] B.D. Michael, P. O'Neill, Science 287 (2000) 1603.
[56] V.E. Cook, R.K. Mortimer, Radiat. Res. 125 (1991) 102.
[57] C.M. deLara, M.A. Hill, T.J. Jenner, D. Papworth, P. O'Neill, Radiat. Res. 155 (2001) 440.
[58] E. Höglund, E. Blomquist, J. Carlsson, B. Stenerlöw, Int. J. Radiat. Biol. 76 (2000) 539.
[59] H.C. Newman, K.M. Prise, M. Folkard, B.D. Michael, Int. J. Radiat. Biol. 71 (1997) 347.
[60] M. Löbrich, P.K. Cooper, B. Rydberg, Int. J. Radiat. Biol. 70 (1996) 493.
[61] H. Tomita, M. Kai, T. Kusama, Y. Aoki, A. Ito, Int. J. Radiat. Biol. 66 (1994) 669.
[62] R. Roots, S. Okada, Radiat. Res. 64 (1975) 306.
[63] A.A. Valota et al., in preparation.
[64] J. Fulford, P. Bonner, D.T. Goodhead, M.A. Hill, P. O'Neill, J. Phys. Chem. A 103 (1999) 11345.
[65] A. Yokoya, R. Watanabe, T. Hara, J. Radiat. Res. 40 (1999) 145.
[66] K. Hieda, T. Hirono, A. Azami, M. Suzuki, Y. Furusawa, H. Maezawa, N. Usami, A. Yokoya, K. Kobayashi, Int. J. Radiat. Biol. 70 (1996) 437.
[67] K.M. Prise, G. Ahnströhm, M. Belli, J. Carlsson, D. Frankenberg, J. Kiefer, M. Löbrich, B.D. Michael, J. Nygren, G. Simone, B. Stenerlöw, Int. J. Radiat. Biol. 74 (1998) 173.
[68] A. Cole, R.E. Meyn, R. Chen, P.M. Corry, W. Hittelman, Mechanisms of cell injury, in: R.E. Mayn, H.R. Withers (Eds.), Radiation Biology in Cancer Research, New York, 1980, p. 33.
[69] J.F. Ward, W.F. Blakely, E.I. Joner, Radiat. Res. 103 (1985) 383.
[70] K.M. Prise, M. Folkard, S. Davies, B.D. Michael, Radiat. Res. 117 (1989) 489.
[71] D. Frankenberg, D.T. Goodhead, M. Frankenberg-Schwager, R. Harbich, D.A. Bance, R.E. Wilkinson, Int. J. Radiat. Biol. 50 (1986) 727.